

LETTERS

Nanoscale chemical imaging of a working catalyst by scanning transmission X-ray microscopy

Emiel de Smit¹, Ingmar Swart¹, J. Fredrik Creemer², Gerard H. Hoveling³, Mary K. Gilles⁴, Tolek Tyliczszak⁴, Patricia J. Kooyman⁵, Henny W. Zandbergen⁶, Cynthia Morin¹, Bert M. Weckhuysen¹ & Frank M. F. de Groot¹

The modern chemical industry uses heterogeneous catalysts in almost every production process¹. They commonly consist of nanometre-size active components (typically metals or metal oxides) dispersed on a high-surface-area solid support, with performance depending on the catalysts' nanometre-size features and on interactions involving the active components, the support and the reactant and product molecules. To gain insight into the mechanisms of heterogeneous catalysts, which could guide the design of improved or novel catalysts, it is thus necessary to have a detailed characterization of the physicochemical composition of heterogeneous catalysts in their working state at the nanometre scale^{1,2}. Scanning probe microscopy methods have been used to study inorganic catalyst phases at subnanometre resolution^{3–6}, but detailed chemical information of the materials in their working state is often difficult to obtain^{5–7}. By contrast, optical microspectroscopic approaches offer much flexibility for *in situ* chemical characterization; however, this comes at the expense of limited spatial resolution^{8–11}. A recent development promising high spatial resolution and chemical characterization capabilities is scanning transmission X-ray microscopy^{4,12,13}, which has been used in a proof-of-principle study to characterize a solid catalyst¹⁴. Here we show that when adapting a nanoreactor specially designed for high-resolution electron microscopy⁷, scanning transmission X-ray microscopy can be used at atmospheric pressure and up to 350 °C to monitor *in situ* phase changes in a complex iron-based Fischer–Tropsch catalyst and the nature and location of carbon species produced. We expect that our system, which is capable of operating up to 500 °C, will open new opportunities for nanometre-resolution imaging of a range of important chemical processes taking place on solids in gaseous or liquid environments.

In situ solid-state microscopic catalyst characterization studies that use scanning transmission electron microscopy/electron energy-loss spectroscopy^{3,4}, scanning tunnelling microscopy^{5,6} or optical microspectroscopic techniques^{8–11} focus either on identifying the inorganic catalyst phase responsible for the catalytic activity, or on characterizing organic reactants, intermediates and products interacting with the catalyst surface. Scanning transmission X-ray microscopy (STXM) is a particularly promising recent addition to the field of chemical microspectroscopy^{4,12,13} in that the use of soft X-rays (200–2,000 eV) as a probe makes it possible to image both the active phase of the catalyst (through absorption edges of the inorganic species) and the organic reactant phase of the catalyst (through the absorption edges of carbon, oxygen and nitrogen) with a spatial resolution of ~15 nm. In addition, the X-ray probe induces less radiation damage in comparison with the related scanning transmission electron microscopy/electron energy-loss spectroscopy technique⁴.

The main experimental challenge to overcome when applying the technique *in situ* is the strong attenuation of soft X-rays by matter. As a result, stringent restrictions apply to the thickness of the sample and the X-ray path length through the medium. For example, the transmission of 700-eV X-rays through 1-bar CO decreases from 60% after 50 µm to ~0.1% after 250 µm. This difficulty meant that the first study¹⁴ of a catalytic solid using STXM under *in situ* conditions was restricted to sample treatments in diluted gases at temperatures below 260 °C, which precluded the study of many catalytic systems. For the present work, we adapt a nanoreactor originally designed for *in situ* transmission electron microscopy studies⁷ for use in STXM and are thus able to expose our sample to a reactant gas atmosphere (typically 1.2 bar) at temperatures up to 500 °C. In addition, as gas-phase attenuation for STXM is lower than in transmission electron microscopy experiments⁴, the nanoreactor allows the use of CO in the *in situ* STXM experiments.

The nanoreactor, manufactured as a microelectromechanical system, consists of a reactor chamber connected by micrometre-size gas-flow channels (see Fig. 1 for details of the set-up). Two amorphous 1.2-µm-thick SiN_x windows separate the reactor from the outer environment. The windows are etched down to a thickness of 10 nm in certain areas to maximize the transmission of the soft X-rays. The height of the reactor is about 50 µm and ensures minimum attenuation of the X-rays by gas-phase molecules. Heating is provided by a platinum resistive heater spiral embedded in one of the windows⁷. The reactor is supported on an adaptor which is mounted on an interferometrically controlled, piezoelectric stage that can translate the sample in the X-ray beam with nanometre precision. The adaptor is designed to hold up to two separate nanoreactors and connects the reactors to the external gas supply and electronics.

We use the system for an *in situ* STXM study of a fully promoted iron-based Fischer–Tropsch catalyst. In Fischer–Tropsch synthesis (FTS), synthesis gas (a mixture of CO and H₂) is converted into hydrocarbon chains through a surface polymerization reaction^{15–17}. This reaction enables the production of high-purity chemicals and transportation fuels from sources other than conventional crude oil, most notably natural gas, coal and biomass. The iron-based catalyst consists of an iron oxide phase dispersed on silicon oxide (SiO₂), with copper oxide and potassium oxide promoters added to improve its selectivity, activity and stability. During FTS, iron oxide and metallic iron (α-Fe) usually coexist, with the iron phases largely converted into iron carbides (essentially α-Fe species with carbon dissolved in their interstitial vacancies). Owing to the complexity of the iron–oxygen–carbon system, the identity of the active phase(s) has long been controversial. In fact, α-Fe, bulk and surface iron carbides and Fe₃O₄ have all been suggested as active phases for FTS¹⁷.

¹Inorganic Chemistry and Catalysis, Debye Institute for Nanomaterials Science, Utrecht University, Sorbonnelaan 16, 3584 CA Utrecht, The Netherlands. ²DIMES-ECTM, Delft University of Technology, PO Box 5053, 2600 GB Delft, The Netherlands. ³DEMO, Delft University of Technology, PO Box 5031, 2600 GA Delft, The Netherlands. ⁴Advanced Light Source, Lawrence Berkeley National Laboratory, Berkeley, California 94720, USA. ⁵DelftChemTech and National Centre for High Resolution Electron Microscopy, Delft University of Technology, Julianalaan 136, 2628 BL Delft, The Netherlands. ⁶Kavli Institute of NanoScience, National Centre for High Resolution Electron Microscopy, Delft University of Technology, PO Box 5046, 2600 GA Delft, The Netherlands.

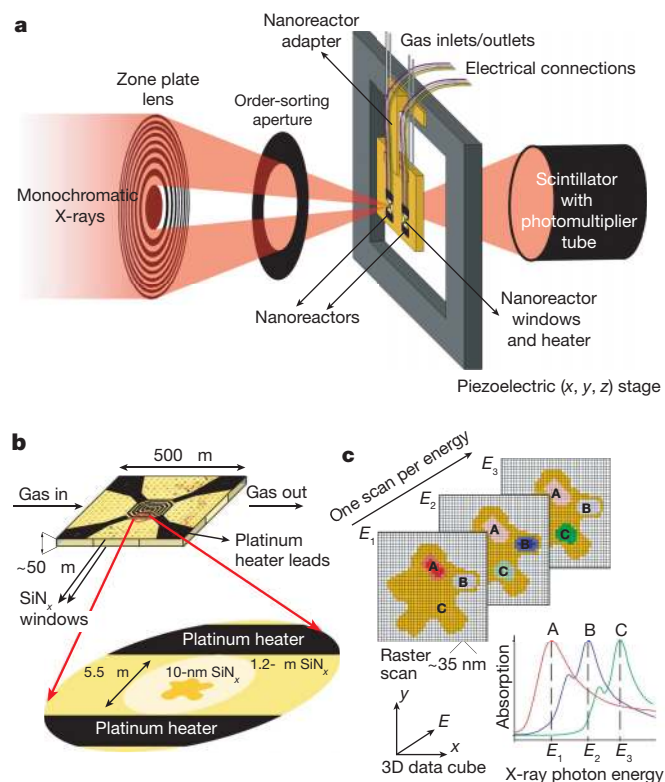


Figure 1 | Experimental set-up and data acquisition method. **a**, Diagram of the *in situ* STXM technique. Soft X-ray light is focused on the sample using a Fresnel-type zone plate lens. An order-sorting aperture filters out higher-order diffraction orders. The nanoreactor containing the sample is placed in an adaptor that holds up to two nanoreactors at the same time. The adaptor can be translated with nanometre precision by an interferometrically controlled (x, y, z) piezoelectric stage, allowing the acquisition of raster scans. **b**, Close-up of the nanoreactor, showing the windows and the embedded heater spiral⁷. The reactor dimensions are $\sim 500 \times 500 \times 50 \mu\text{m}^3$. The platinum heater has four electronic connections for simultaneous power supply and resistive temperature measurement. The sample itself is supported on the SiN_x windows. The measurements are performed in the circular areas ($5.5\text{-}\mu\text{m}$ diameter) where the $1.2\text{-}\mu\text{m}$ -thick SiN_x windows are etched down to a thickness of $\sim 10\text{ nm}$. **c**, Diagram of a typical STXM data acquisition method. By acquiring images at different X-ray photon energies (for example E_1 , E_2 and E_3), a three-dimensional (3D) data cube with full spectral information at every pixel is obtained. This data can be used to image and distinguish between specific chemical species (for example species A, B and C).

In our experiment, we image the reduction of supported iron oxide particles upon heating to 350°C in H_2 (1 bar) and, subsequently, the working catalyst during the FTS reaction at 250°C in synthesis gas (1 bar).

We use the carbon K edge (284.2 eV), the oxygen K edge (543.1 eV) and the iron L_2 and L_3 edges (706.8 eV and 719.9 eV , respectively) to image and characterize the sample. The iron L_2 and L_3 edges are used to monitor the valence and coordination^{18,19} of iron species, and the oxygen K edge is used to distinguish between different oxygen-containing species. The pre-edge in the oxygen K-edge spectrum is due to the mixing of the oxygen $2p$ states with transition metal $3d$ states and can be used as a measure for the unoccupied iron $3d$ states²⁰. In addition, the oxygen K edge of SiO_2 is sufficiently distinct from the iron oxide spectra to specifically map the location of the silicon and iron oxide species. The carbon K edge is measured to image the type and location of carbon species present in the catalyst during reaction.

Before the *in situ* experiments, we analyse the material at room temperature (25°C) in a helium atmosphere by recording images at the iron L_2 and L_3 edges (Fig. 2d) and the oxygen K edge (Fig. 2e). The iron phase is mainly present as $\alpha\text{-Fe}_2\text{O}_3$, as is made evident by X-ray

absorption spectra of the iron L_2 and L_3 edges and the oxygen K edge^{18–20}. Quantitative analysis by linear-combination fitting of the oxygen K-edge spectrum shows that the $\alpha\text{-Fe}_2\text{O}_3$ phase contributes 25% of the spectrum, whereas SiO_2 contributes 75%. Distinct regions are found in which there is no absorption at the iron L_2 and L_3 edges and strong absorption at the oxygen K edge. The oxygen K edge of these regions is characteristic of the SiO_2 phase^{21,22}. No significant contribution of carbon species is observed in the starting material. By fitting the experimental spectrum to a linear combination of the spectra of the pure phases, we construct composite contour maps, as shown in Fig. 2a for SiO_2 and Fe_2O_3 .

After a 2-h exposure to H_2 at 350°C , the material shows significant changes. Figure 2b is a composite contour map of the region in Fig. 2a. Analysis of the iron L_2 and L_3 edges (Fig. 2f) and the oxygen K edge (Fig. 2g) of the two regions indicated in Fig. 2b shows that the Fe_2O_3 is converted into a mixture of iron oxides and metallic iron. The iron L_3 edges show an enhanced intensity at 707.7 eV , which is attributed to the occurrence of Fe^{2+} species in octahedral coordination^{18,19}. These observations suggest the formation of Fe_3O_4 and an octahedral Fe^{2+} system, probably Fe_2SiO_4 . Because the intensity ratio of the Fe^{2+} peak to the Fe^{3+} peak is higher than would be expected for Fe_3O_4 (ref. 18), the feature is assigned to the occurrence of Fe_2SiO_4 . From the spectra alone, it is not possible to distinguish between Fe_2SiO_4 and other octahedral Fe^{2+} oxides, such as FeO . However, it has been reported that a reaction between FeO and the SiO_2 support can cause the loss of iron species into the support during the activation treatment and FTS^{23,24}. In addition, under our reaction conditions FeO is expected to disproportionate into Fe_3O_4 and Fe^0 species²⁵.

Apart from the spectral contributions of the Fe_3O_4 and Fe_2SiO_4 phases, there is also a small contribution observed at 706.8 eV , corresponding to the occurrence of Fe^0 species. The iron L_2 - and L_3 -edge spectra are analysed quantitatively by least-squares fitting with reference spectra. The calculated phase composition of the selected particle from linear combination fitting is 25% Fe^0 , 25% Fe_2SiO_4 and 50% Fe_3O_4 for region one and 33% Fe^0 , 50% Fe_2SiO_4 and 17% Fe_3O_4 for region two (these regions are shown in Fig. 2b, c). The pre-edge intensity of the oxygen K edge (Fig. 2g) of both regions decreased significantly, which is due to (1) the decreased overlap between iron and oxygen states with lower valences and (2) the reduction to Fe^0 , implying less oxidic iron. The total contribution of iron oxide phases to the oxygen K-edge spectrum decreases from 20% to 10%. As can be seen in Fig. 2a, b, the size and shape of the particle change significantly, indicating morphological changes in the sample as a result of the transition from Fe_2O_3 to Fe_3O_4 , Fe_2SiO_4 and Fe^0 .

During the subsequent FTS reaction in synthesis gas at 250°C , the Fe_3O_4 phase is further converted to Fe^0 and Fe_2SiO_4 . Figure 2c shows the chemical composite contour map of the selected region after 4 h of FTS. The iron L_3 edge of the selected regions (Fig. 2h) shows an increase in the intensity of the feature at 707.7 eV . The pre-edge in the oxygen spectrum (Fig. 2i) is almost absent in these regions. The spectrum mainly shows a contribution from SiO_2 , plus a shoulder at the edge (as indicated by the arrows) indicating strong interaction between small iron particles and the SiO_2 support²⁶. Quantitative analysis of the iron L_2 and L_3 edges acquired from region one show a phase composition of 20% Fe^0 , 75% Fe_2SiO_4 and 5% Fe_3O_4 . Region two has a composition of approximately 40% Fe^0 , 50% Fe_2SiO_4 and 10% Fe_3O_4 . Analysis of the carbon K edge shows that carbon is preferentially present in iron-rich regions (Fig. 3). Furthermore, regions of higher Fe^0 intensity have carbon K-edge spectra different than those of regions of lower Fe^0 intensity. The high contribution of the absorption band at 285 eV in the carbon K-edge spectrum (Fig. 3a), corresponding to the $1s \rightarrow \pi^*$ transition, indicates the presence of sp^2 hybridized carbon species in the iron-rich region²⁷. This observation, in combination with the almost featureless absorption band due to the $1s \rightarrow \sigma^*$ transition at $\sim 295\text{ eV}$, suggests that the iron phase is converted to iron carbide²⁸. In the regions where less iron is

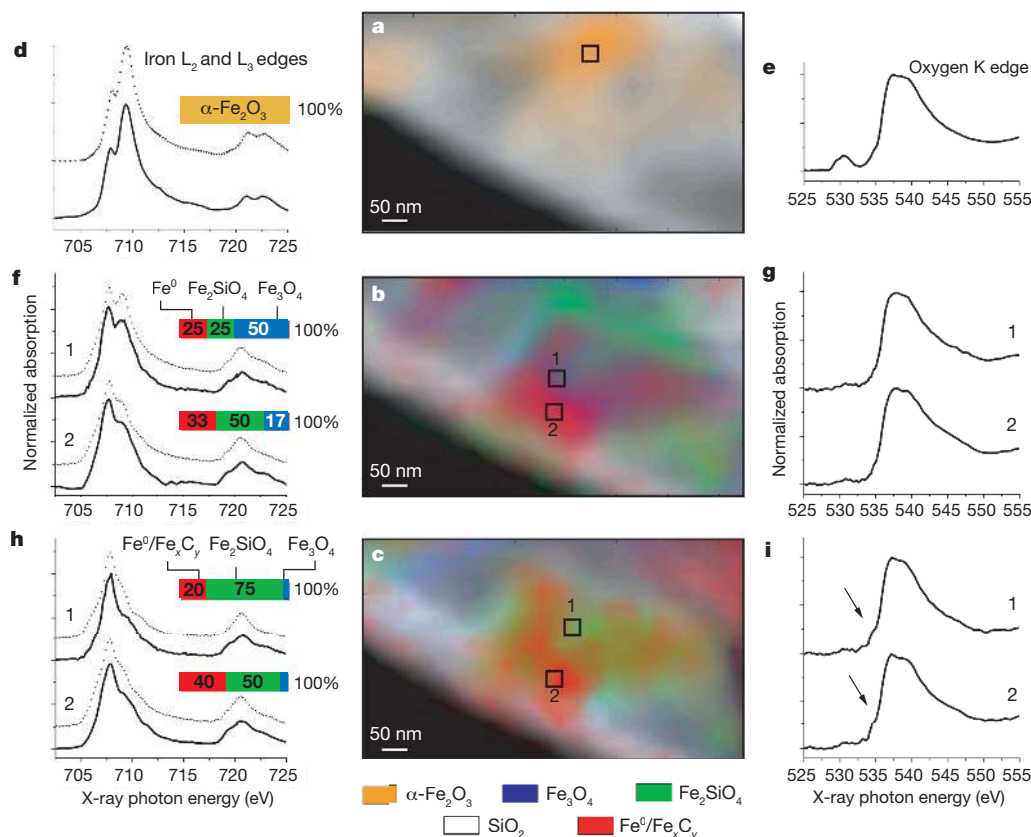


Figure 2 | Chemical contour maps and X-ray absorption spectra of the catalyst material during the different stages of reaction. Chemical contour maps (a, b, c) of a 400 nm × 750 nm region and corresponding iron L₂- and L₃-edge (d, f, h) and oxygen K-edge (e, g, i) X-ray absorption spectra, all normalized to a maximum absorption of one. The contour lines have been removed for clarity. a, Before treatment, at room temperature (25 °C) in helium; b, after 2 h in H₂ at 350 °C; c, after 4 h in synthesis gas at 250 °C.

Specific sampling regions and the corresponding X-ray absorption spectra are indicated in the figures. The dotted lines in d, f and h indicate the spectra fitted by a linear combination of reference spectra. The bar graphs represent the calculated relative percentage contributions of the different iron phases at the sampling points. The arrows in i indicate the observed shoulder feature.

present, the $1s \rightarrow \pi^*$ absorption peak is lower in intensity and less sharp, suggesting a more sp^3 -like character²⁷ (Fig. 3b), which can be attributed to the FTS reaction products. Furthermore, an additional peak at 288 eV, characteristic of carboxylic species²⁷, is observed. The presence of reactant carbon species in iron-deficient areas indicates that the support might have some role in the spillover of (hydro)-carbon species from the metal to the support, thereby preventing blocking of the active sites of the catalyst.

These observations demonstrate that STXM can image a catalytic system as complex as an iron-based Fischer–Tropsch catalyst under catalytically relevant reaction conditions, and deliver detailed information on the morphology and composition of the catalyst material. We anticipate that improvements in the optics and imaging methods used with the X-ray microscope will result in a higher achievable spatial resolution²⁹, and that further development of the detection techniques will improve the count rates to the degree that it might be possible to carry out time-resolved experiments. Moreover, improved designs of dedicated reactor cells may enable studies at higher pressures and temperatures and/or X-ray tomography applications^{4,30}. In short, *in situ* STXM is a promising technique that we expect to develop and deliver new insights into many complex chemical problems.

METHODS SUMMARY

Materials. The promoted iron-based Fe₂O₃/CuO/K₂O/SiO₂ Fischer–Tropsch catalyst was synthesized following a previously reported procedure¹⁵. The catalyst material was ground, suspended in ethanol, treated in an ultrasonic bath and

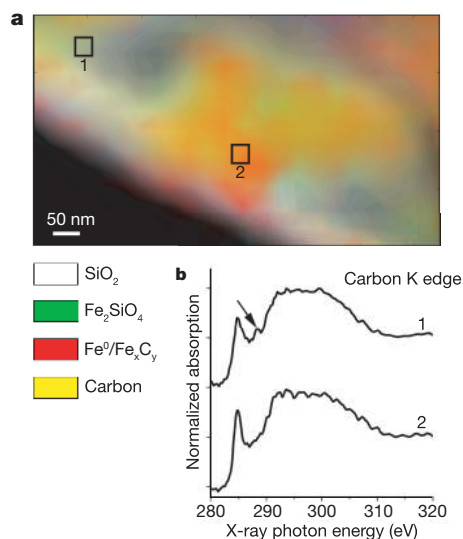


Figure 3 | Location and nature of carbon species on the catalyst material. a, Chemical contour map of the 400 nm × 750 nm region of the catalyst material represented in Fig. 2, showing the distribution of carbon species after 4 h in synthesis gas at 250 °C, overlaid on the iron species map. b, Carbon K-edge spectra corresponding to the indicated sample regions. The arrow indicates the additional peak at 288 eV.

loaded into the nanoreactor by flowing the suspension through the reactor. Remaining ethanol was removed from the reactor by drying at room temperature. **Chemical imaging.** All experiments were performed on the interferometrically controlled STXM microscope at beamline 11.0.2 (ref. 13) of the Advanced Light Source at the Lawrence Berkeley National Laboratory, USA. As a compromise between spatial resolution and the longer working distance required, a 35-nm zone plate lens was used with a spatial resolution of ~ 40 nm. The X-ray absorption spectra and the images were measured with a $35\text{ nm} \times 35\text{ nm}$ step size of the piezoelectric sample stage.

Data analysis. STXM data files were analysed using the aXis2000 software package (<http://unicorn.mcmaster.ca/aXis2000.html>), which allowed detailed interactive processing of the images and least-squares linear-combination fitting of the X-ray absorption spectra.

Full Methods and any associated references are available in the online version of the paper at www.nature.com/nature.

Received 29 June; accepted 24 September 2008.

1. Bell, A. T. The impact of nanoscience on heterogeneous catalysis. *Science* **299**, 1688–1691 (2003).
2. Weckhuysen, B. M. Chemistry: Catalysts live and up close. *Nature* **439**, 548 (2006).
3. Hansen, T. W. *et al.* Atomic-resolution in situ transmission electron microscopy of a promoter of a heterogeneous catalyst. *Science* **294**, 1508–1510 (2001).
4. Hitchcock, A. P., Dynes, J. J., Johansson, G., Wang, J. & Botton, G. Comparison of NEXAFS microscopy and TEM-EELS for studies of soft matter. *Micron* **39**, 311–319 (2008).
5. Zambelli, T., Barth, J. V., Wintterlin, J. & Ertl, G. Complex pathways in dissociative adsorption of oxygen on platinum. *Nature* **390**, 495–497 (1997).
6. Frenken, J. & Hendriksen, B. The reactor-STM: A real-space probe for operando nanocatalysis. *MRS Bull.* **32**, 1015–1021 (2007).
7. Creemer, J. F. *et al.* Atomic-scale electron microscopy at ambient pressure. *Ultramicroscopy* **108**, 993–998 (2008).
8. Roelfaers, M. B. J. *et al.* Spatially resolved observation of crystal-face-dependent catalysis by single turnover counting. *Nature* **439**, 572–575 (2006).
9. Zurner, A., Kirstein, J., Doblinger, M., Brauchle, C. & Bein, T. Visualizing single-molecule diffusion in mesoporous materials. *Nature* **450**, 705–708 (2007).
10. Kox, M. H. F., Stavitski, E. & Weckhuysen, B. M. Nonuniform catalytic behavior of zeolite crystals as revealed by in situ optical microspectroscopy. *Angew. Chem. Int. Ed.* **46**, 3652–3655 (2007).
11. Stavitski, E., Kox, M. H. F., Swart, I., de Groot, F. M. F. & Weckhuysen, B. M. In situ synchrotron-based IR microspectroscopy to study catalytic reactions in zeolite crystals. *Angew. Chem. Int. Ed.* **47**, 3543–3547 (2008).
12. Warwick, T. *et al.* A scanning transmission X-ray microscope for materials science spectromicroscopy at the Advanced Light Source. *Rev. Sci. Instrum.* **69**, 2964–2973 (1998).
13. Kilcoyne, A. L. D. *et al.* Interferometer-controlled scanning transmission X-ray microscopes at the Advanced Light Source. *J. Synchrotron Radiat.* **10**, 125–136 (2003).
14. Drake, I. J. *et al.* An in situ cell for characterization of solids by soft X-ray absorption. *Rev. Sci. Instrum.* **75**, 3242–3247 (2004).
15. Dry, M. E. in *Catalysis - Science and Technology* (eds Anderson, J. R. & Boudart, M.) 160–255 (Springer, 1981).
16. Van der Laan, G. P. & Beenackers, A. Kinetics and selectivity of the Fischer-Tropsch synthesis: A literature review. *Catal. Rev. Sci. Eng.* **41**, 255–318 (1999).
17. de Smit, E. & Weckhuysen, B. M. The renaissance of iron-based Fischer-Tropsch synthesis: On the multifaceted catalyst deactivation behaviour. *Chem. Soc. Rev.* doi:10.1039/B805427D (in the press).
18. Heijboer, W. M. *et al.* In-situ soft X-ray absorption of over-exchanged Fe/ZSM5. *J. Phys. Chem. B* **107**, 13069–13075 (2003).
19. de Groot, F. & Kotani, A. *Core Level Spectroscopy of Solids* (Taylor & Francis, 2008).
20. de Groot, F. M. F. *et al.* Oxygen 1s x-ray-absorption edges of transition-metal oxides. *Phys. Rev. B* **40**, 5715–5723 (1989).
21. Sharp, T. *et al.* Distinction between six- and fourfold coordinated silicon in SiO₂ polymorphs via electron loss near edge structure (ELNES) spectroscopy. *Phys. Chem. Miner.* **23**, 17–24 (1996).
22. Davoli, I. *et al.* Structure of densified vitreous silica: Silicon and oxygen XANES spectra and multiple scattering calculations. *Phys. Chem. Miner.* **19**, 171–175 (1992).
23. Wielers, A. F. H., Kock, A. J. H. M., Hop, C. E. C. A., Geus, J. W. & van der Kraan, A. M. The reduction behavior of silica-supported and alumina-supported iron catalysts: A Mössbauer and infrared spectroscopic study. *J. Catal.* **117**, 1–18 (1989).
24. Zhang, C. H., Wan, H. J., Yang, Y., Xiang, H. W. & Li, Y. W. Study on the iron-silica interaction of a co-precipitated Fe/SiO₂ Fischer-Tropsch synthesis catalyst. *Catal. Commun.* **7**, 733–738 (2006).
25. Jozwiak, W. K., Kaczmarek, E., Maniecki, T. P., Ignaczak, W. & Maniukiewicz, W. Reduction behavior of iron oxides in hydrogen and carbon monoxide atmospheres. *Appl. Catal. A Gen.* **326**, 17–27 (2007).
26. Wang, F., Malac, M. & Egerton, R. F. Alternative methods of identifying the oxidation of metallic nanoparticles embedded in a matrix. *Micron* **38**, 371–376 (2007).
27. Braun, A. *et al.* Advantages of soft X-ray absorption over TEM-EELS for solid carbon studies - a comparative study on diesel soot with EELS and NEXAFS. *Carbon* **43**, 117–124 (2005).
28. Urbonaitė, S. *et al.* EELS studies of carbide derived carbons. *Carbon* **45**, 2047–2053 (2007).
29. Thibault, P. *et al.* High-resolution scanning X-ray diffraction microscopy. *Science* **321**, 379–382 (2008).
30. Le Gros, M. A., McDermott, G. & Larabell, C. A. X-ray tomography of whole cells. *Curr. Opin. Struct. Biol.* **15**, 593–600 (2005).

Acknowledgements We acknowledge financial support for this research work from the Dutch National Science Foundation in the form of two VICI grants (to F.M.F.d.G. and B.M.W.), a grant from the Netherlands Research School Combination on Catalysis (to B.M.W. and F.M.F.d.G.) and a grant from Shell Global Solutions (to B.M.W.). The Advanced Light Source is supported by the Director, Office of Science, Office of Basic Energy Sciences, US Department of Energy. The nanoreactors were fabricated with the assistance of the DIMES ICP-group and the Nanofacility of TU Delft.

Author Information Reprints and permissions information is available at www.nature.com/reprints. Correspondence and requests for materials should be addressed to F.M.F.d.G. (f.m.f.degroot@uu.nl) or B.M.W. (b.m.weckhuysen@uu.nl).

METHODS

Catalyst material preparation. The $\text{Fe}_2\text{O}_3/\text{CuO}/\text{K}_2\text{O}/\text{SiO}_2$ catalyst was prepared by precipitation from a ferric nitrate solution using a basic sodium carbonate solution¹⁵. We dissolved 25 g $\text{Fe}(\text{NO}_3)_3 \cdot 9\text{H}_2\text{O}$ (98+% ACS reagent, Acros) and 1.2 g $\text{Cu}(\text{NO}_3)_2 \cdot 3\text{H}_2\text{O}$ (p.a. 99.5%, Merck) in 100 ml distilled water. The solution was heated to near its boiling point, after which it was slowly (over ~ 1 min) added to a vigorously stirred, near-boiling solution of 25 g Na_2CO_3 in 100 ml distilled water. As sodium has been reported to negatively influence the catalytic performance of the catalysts, the resulting precipitate was filtered and reslurried in about 1 l of near-boiling distilled water to remove any residual sodium. This process was repeated about four times, until the pH of the solution was about 7.

The washed precipitate was reslurried in 200 ml distilled water. About 8 g of potassium water-glass solution ($\text{K}_2\text{O}/\text{SiO}_2$ (1:2.15), Akzo-PQ) was added to the slurry under vigorous stirring and 1.5 ml of concentrated HNO_3 was added to precipitate the SiO_2 and lower the total potassium content. After this, the precipitate was dried for ~ 6 h at 60°C and subsequently for 24 h at 120°C . Finally, the material was calcined in a flow of air at 300°C for 5 h using a heating ramp of 5°C .

The final catalyst compositions were confirmed by X-ray fluorescence analysis using a Goffin Meyvis Spectro X-lab 2000. The relative molar composition of the catalyst was Fe:Cu:K:Si 100:7.5:5.9:15.6.

Nanoreactor and adaptor design. The design and assembly of the nanoreactor itself is described in more detail elsewhere⁷. The nanoreactor adaptor was fabricated from a solid slab of brass. Holes accommodating the 1/16-inch gas tubing were drilled into the brass slab and connected to the nanoreactors from their rear side. Each nanoreactor sits on top of a gas channel inlet and outlet, which were sealed using Viton O rings. The nanoreactors are held in place by a cover plate. Electronic connections, four for each reactor, were connected to the nanoreactor by means of the wire bonding method, using aluminium wires.

STXM data analysis. Chemical contour maps and the relative iron phase compositions were acquired by using the aXis2000 software package (<http://unicorn.mcmaster.ca/aXis2000.html>). The software uses linear regression to fit the absorbance (A) spectrum of each ($35 \times 35 \text{ nm}^2$) pixel to a linear combination of reference spectra. Absorbance is defined as $A = -\log_{10}(I/I_0)$, where I and I_0 respectively denote the transmitted and incident intensities. The fit procedure minimizes $(A_{x,y,E}^{\text{measured}} - A_{x,y,E}^{\text{calculated}})^2$ over an energy range, where $A_{x,y,E}^{\text{measured}}$ is the absorbance measured at point (x, y) and energy E and $A_{x,y,E}^{\text{calculated}}$ is defined as

$$A_{x,y,E}^{\text{calculated}} = \text{const}_E + a_{1,E}A_{1,E} + a_{2,E}A_{2,E} + \dots + a_{i,E}A_{i,E}$$

Here const_E is a constant, $A_{i,E}$ is the absorbance of compound i at energy E and $a_{i,E}$ is the expansion coefficient of compound i at that energy. The coefficients are varied to fit the measured spectrum.